



Article

# Dissolution of Microalloying Elements in a Ladle Metallurgy Furnace

Ogochukwu Queeneth Duruiheme, Xipeng Guo, Nicholas Walla and Chenn Zhou \*

Center for Innovation through Visualization and Simulation (CIVS) and Steel Manufacturing Simulation and Visualization Consortium (SMSVC), Purdue University Northwest, Hammond, IN 46323, USA

\* Correspondence: czhou@pnw.edu; Tel.: +1-219-989-2665

Abstract: Industrial fusion of microalloying elements in steelmaking is imperative in defining and optimizing certain steel properties due to their strengthening and significant grain refinements effects at minute quantities. Copper, vanadium, and columbium are explored in this investigation to monitor their respective dissolution processes in a ladle metallurgy furnace (LMF), with concise parametric studies on effects of number of plugs and variations in argon gas flow rates for stirring. To track particle disintegration in the molten bath inside, intricate numerical processing was carried out with the use of mathematical models and to simulate the mixing process; turbulent multiphase computational fluid dynamics (CFD) models were combined with a user-defined function. The numerical findings highlight the connection between mixing time and gas blowing since the quantity of stirring plugs employed and the gas flow rates directly affect mixing effectiveness. The amount of particles to be injected and their total injection time were validated using industrial measurement; an average difference of 9.9% was achieved. In order to establish the need for an exceptionally high flow rate and inevitably reduce resource waste, extreme charging of flow rates for gas stirring were compared to lesser gas flow rates in both dual- and single-plug ladles. The results show that a single-plug ladle with a flow rate of 0.85 m<sup>3</sup>/min and a dual-plug ladle with a total flow rate of 1.13 m<sup>3</sup>/min have the same mixing time of 5.6 min, which was the shortest among all scenarios.

**Keywords:** injection metallurgy; ladle homogenization; alloy addition; alloy recovery



Citation: Duruiheme, O.Q.; Guo, X.; Walla, N.; Zhou, C. Dissolution of Microalloying Elements in a Ladle Metallurgy Furnace. *Metals* 2023, 13, 421. https://doi.org/10.3390/met13020421

Academic Editor: Carlos Capdevila-Montes

Received: 20 January 2023 Revised: 11 February 2023 Accepted: 13 February 2023 Published: 17 February 2023



Copyright: © 2023 by the authors. Licensee MDPI, Basel, Switzerland. This article is an open access article distributed under the terms and conditions of the Creative Commons Attribution (CC BY) license (https://creativecommons.org/licenses/by/4.0/).

## 1. Introduction

To produce different steel grades, ladle metallurgy furnaces (LMF) are widely used in refining operations during secondary steelmaking processes. Figure 1 summarized the schematic of the alloy injecting process. Using alloy addition, electrical reheating to the desired temperature, desulphurization, and flotation of the inclusions created during steel deoxidation, this unit system makes it possible to modify the chemical composition of steel. The process of basic alloying is often carried out during tapping, when the kinetic energy of the tapping stream is used to accelerate the melting and homogenization of alloys in the ladle. However, due to the availability of technologies for controlled additions based on steel sampling and analysis, modest additions are still made during ladle treatments [1]. The first stage in integrating these cutting-edge methods in steel production is argon blowing.

In order to speed up the rates of various process-controlled heat and mass transfer phenomena, such as the distribution of heat from the arc, alloy and lime dissolution and mixing, the slag-metal reaction, and inclusion flotation, among others, gas stirring or blowing is used during the metallurgy process [2]. However, how much or how big of a gas bubble is injected during the injection procedure determines the process. Additionally, by accelerating convective diffusion and heat transfer rates during mixing, the intensity of the churning produces homogeneity. Extensive alloy addition methods have been studied experimentally and numerically throughout the years [2–10].

Metals 2023, 13, 421 2 of 19

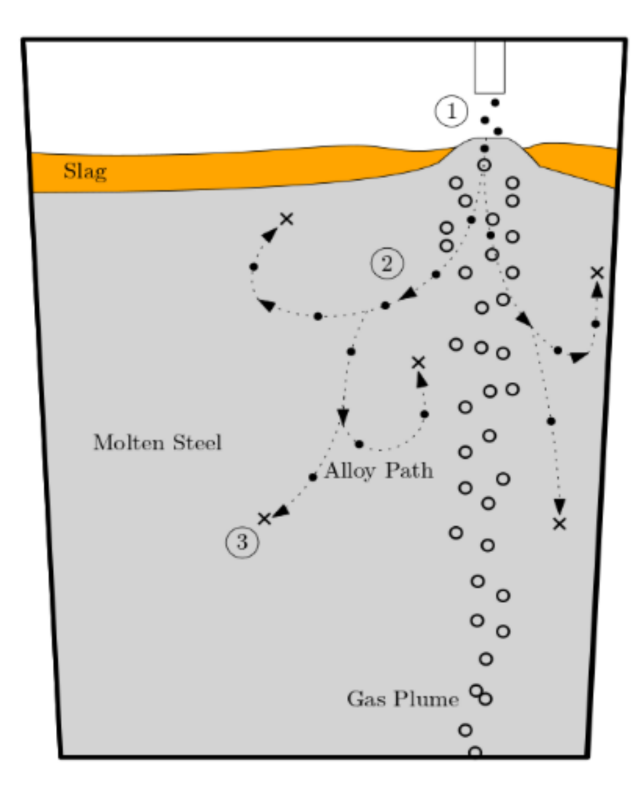


Figure 1. Injection process: (1) alloy entrance; (2) shell formation and melting; (3) dissolution.

The quality of the steel is determined by the uniform distribution of the alloying components, making the dissolution of alloy materials in liquid steel an essential step in secondary metallurgy. During mixing, a few variables significantly influenced by the steel temperature and starting flow conditions are made clear. Tensile strength, hardenability, ductility, and corrosion resistance of steel are modified by certain alloys that are specifically employed for their enhancing qualities and deoxidation ability. Their lower melting points and densities also aid in efficient stirring, but because they cannot penetrate the slag layer, lower-density additions might transfer to the slag rather than the metal. The temperature of the steel may be lowered if higher-density alloys sink to the bottom of the ladle, where there is less movement [11]. According to Aden Boer's theory, introducing particles with a wide size distribution may cause segregation and make the steel melt around it, resulting in a heat sink [3].

Due to low liquidus temperature and the formation of a steel shell as a result of particle integration into the bath, the alloy may melt inside the shell. According to D. Webber [11], who describes shell's formation in his experimental work, the size and hydrodynamics of the alloys in the ladle, as well as their physical and chemical properties, all have an impact on how well they are incorporated into the melt. Most often, alloy addition causes a steel shell to solidify on the surface of the cold alloy. The shell is then melted, and the alloy is released into the bath. The alloy dissolution process is affected by both mass transfer and heat transfer. The duration of the shell's existence and the amount of heat transferred from the melt to the particle when the shell is still present within the melt are addressed by Zhang and Oeters' [5] mathematical models, which are based on the description of melting, dissolution, and mixing processes without considering chemical reaction.

CFD analysis showed that time required to melt back the first solidified steel shell around the submerged pieces accounts for the majority of the observed dissolution time in a steel melt. For some alloys, the mass transfer process that occurs after the first produced steel shell melts back completely regulates the dissolution kinetics in addition to the steel shell's process of melting back [9]. When examining dissolution or the rate at which it occurs, it is important to take into account the size of the injected particles, their melt temperature, the composition of the steel, its temperature, the intensity of the stirring, and

Metals 2023, 13, 421 3 of 19

turbulence. Peaslee et al. relayed that adding bulk alloys frequently results in segregation or uneven recovery, despite the fact that they might aid in slag layer penetration. The dissolving rate can be considerably boosted by decreasing the alloy size [12]. When alloys in various forms, such as lumps, granules, or particles, melt or partially dissolve into the melt, they could still be present as concentrated volumes of solute surrounded by melt. Concentration at a random site most surely does not equal average concentration since they have not been properly blended. Alloy concentrations around the various surfaces should not be higher than average concentration owing to dissolution in a high-temperature melt [13]. Due to the high stirring power, the mixing time also decreases as the rate of alloy transfer increases. However, according to Webber [11], some investigations have demonstrated specific behaviors where the time of mixing does not shorten with greater stirring power. This can be because of misconceptions about the path of dissolution brought on by temperature.

According to a single-fluid experimental and CFD study conducted by Aoki et al. [7] to quantify mixing in a ladle, the discrepancy in alloy melting times results from the superheat's short-term

Due to their ability to dramatically improve steel properties at low concentrations, microalloying elements are investigated in this work for their dissolving and mixing behaviors inside the LMF, revealing high-strength, low-alloy (HSLA) steels. By enhancing grain hardening and refinement, these elements' strengthening effects make microalloyed steels suitable for high-strength applications [14]. Copper (Cu), columbium (Cb, same as niobium, Nb), and vanadium (V) are a few of the elements whose dissolving properties have been examined. A moderate addition of Cu improves atmospheric corrosion resistance and creates precipitation-hardening qualities; nevertheless, a substantial addition of Cu is harmful. With a strong affinity for carbon, Cb stabilizes elements in stainless steels by forming carbides that are evenly distributed throughout the material, further avoiding localized precipitation at grain boundaries. In addition, V enhances strength, hardness, shock, impact, and wear resistance at high temperatures [15].

Different to other research, with this paper, it is the first time the different alloys in difference ladle operation condition are studied. Based on the results, we can conclude which operation condition is preferred. To accurately replicate the dissolving process of each type of alloy, the model developed for this multiphase study determines each alloy's critical time of dissolution and controls the release of particle mass into the bath and their injection time. It is also taken into account how long it takes for the scattered components to reach a specific level or level of homogeneity. Utilizing precise sample points, recoveries of these alloys after a certain amount of time are compared to plant data. ANSYS Fluent 2020 R1 was used to solve numerically the models representing the flow inside the ladle and the turbulence brought on by the movement of the particles.

#### 2. Methodology

In this paper, Navier–Stokes equations and continuity equations are used to compute a three-dimensional multiphase flow field. The volume-of-fluid multiphase model is employed. The standard k-epsilon model is activated in the computational domain; the inert gas bubbles are represented as discrete phase particles. The fluctuation velocity is maintained while the random walk model takes into account the effects of turbulence on the trajectories.

2.1. Governing Equations

2.1.1. Continuous Phase

Conservation of mass:

$$\frac{\partial \rho}{\partial t} + \nabla \cdot \left( \rho \overrightarrow{u} \right) = 0 \tag{1}$$

where  $\rho$  is the density of the mixture, t is time, and  $\overrightarrow{u}$  is the local velocity.

Metals 2023, 13, 421 4 of 19

Momentum:

$$\frac{\partial}{\partial t} \left( \rho \overrightarrow{u} \right) + \nabla \cdot \left( \rho \overrightarrow{u} \overrightarrow{u} \right) = -\nabla p + \nabla \cdot \left[ \mu \left( \nabla \overrightarrow{u} + \left( \nabla \overrightarrow{u} \right)^T \right) \right] + \rho \overrightarrow{g} + F_b$$
 (2)

where p is the local pressure,  $\mu$  is the viscosity,  $\overrightarrow{g}$  is the acceleration due to gravity,  $F_b$  is the force from bubbles.

Turbulence model:

Standard k-epsilon model is used to model the turbulence flow in the multiphase system. The transportation equation of turbulence kinetic energy and turbulence dissipation rate are shown below:

$$\frac{\partial}{\partial t}(\rho k) + \nabla \cdot \left(\rho k \overrightarrow{u}\right) = \nabla \cdot \left[\left(\mu + \frac{\mu_t}{\sigma_k}\right) \nabla k\right] + G_k + G_b - \rho \varepsilon \tag{3}$$

$$\frac{\partial}{\partial t}(\rho \varepsilon) + \nabla \cdot \left(\rho \varepsilon \overrightarrow{u}\right) = \nabla \cdot \left[\left(\mu + \frac{\mu_t}{\sigma_{\varepsilon}}\right) \nabla \varepsilon\right] + C_{1\varepsilon} \frac{\varepsilon}{k} (G_k + C_{3\varepsilon} G_k) - C_{2\varepsilon} \rho \frac{\varepsilon^2}{k} \tag{4}$$

where  $G_k$  and  $G_b$  are mean velocity gradient and buoyancy effect in the flow causing the kinetic energy generation.  $\sigma_k$  and  $\sigma_\epsilon$  represent turbulence Prandtl numbers.  $C_{1\epsilon}$ ,  $C_{2\epsilon}$ , and  $C_{3\epsilon}$  are constant.

Species transport model:

When flow reaches a quasi-steady state, the alloys are added into the ladle from the top. The species transport model is used to track the local species distribution and movement when the alloy is dissolved into the steel. The transportation equation of species can be described as:

$$\frac{\partial}{\partial t}(\rho Y_i) + \nabla(\rho \overrightarrow{v} Y_i) = \nabla \cdot \left( \left( \frac{\mu_t}{Sc_t} + \rho D_{i,m} \right) (\nabla Y_i) \right) + S_i \tag{5}$$

where  $Y_i$  is the local mass fraction of species in the continuous liquids;  $D_{i,m}$  is the mass diffusion coefficient for species i in the mixture;  $S_i$  is the source term of species i due to the species addition from alloy;  $Sc_t$  is the turbulent Schmidt number, which is 0.7 by default.

## 2.1.2. Discrete Phase

The discrete phase in the study consist of two parts: an argon bubble and the alloy before dissolution. The discrete phase model (DPM) is employed. It is based on the Euler–Lagrange approach to determine the parcel trajectory by solving force balance as shown below:

$$\frac{d\overrightarrow{v}_p}{dt} = F_D(\overrightarrow{v} - \overrightarrow{v}_p) + \frac{\overrightarrow{g}(\rho_p - \rho)}{\rho_p} + \overrightarrow{F}_{VM} + \overrightarrow{F}_{pressure}$$
 (6)

where  $F_D(\overrightarrow{v} - \overrightarrow{v}_p)$  is drag force, and  $F_D$  can be written as

$$F_D = \frac{3\mu C_D Re}{4\rho_n d_n^2} \tag{7}$$

From above equation, Re is the particle Reynolds number.  $C_D$  is the drag coefficient, referring to Aoki et al. [7].

The injection bubble diameter in the paper is taken as 25% of the maximum bubble [16],

$$d_{p,max} = 0.35 \left(\frac{Q^2}{g}\right)^{0.2} \tag{8}$$

## 2.1.3. Alloy Injection Model

The injection processes can be found in Figure 1. To model the process, a two-stage simulation is performed. After the flow reaches a quasi-steady state, the alloy is injected from the ladle top. The alloy is modeled as a DPM particle. When the alloy dissolves into the steel, the mass carried by DPM is transferred to continuous phase, and DPM particle-tracking is terminated.

Metals 2023, 13, 421 5 of 19

The model predicts that injection takes place only once and consistently over a specific time period. Since the particles are defined as computation points traveling with the stream at the injection point, the movement of the virtual fluid mass is monitored.

The time it takes for the steel shell to melt, allowing the alloy particles to settle/diffuse within the melt and eventually dissolve when introduced into the bath, is defined as its "critical time", or  $t_c$ . This takes into account the displacement around the particle prior to its melting due to the temperature difference between the alloy and steel.

Zhang and Oeters' mathematically developed equation, which was made for the simulation process taking into account the melt's solidification temperature, the alloy particle's beginning temperature, and the melt temperature, shows this occurrence [5].

$$t_c = \frac{Cp\rho_A d_A}{\pi h} \frac{T_S - T_O}{T_M - T_S} \tag{9}$$

Here, h is the heat transfer coefficient. Cp is the specific heat, R is the radius of the ferroalloy particle.  $\rho$  is the density of the ferroalloy.

According to Aoki et al. [7], Whitaker's Nusselt number Nu correlation [17] is used to determine the heat transfer coefficient, h, at the surface of the ferroalloy particle using the Reynolds number Re and Prandtl number Pr.

$$Re = \frac{\rho d_A |u_l - u_A|}{\mu} \tag{10}$$

$$Pr = \frac{C_{pM}\mu}{k_M} \tag{11}$$

$$(Nu - 2) = \left(0.4\text{Re}^{\frac{1}{2}} + 0.06\text{Re}^{\frac{2}{3}}\right) Pr^{0.4}$$
 (12)

$$h = \frac{Nuk_M}{d_A} \tag{13}$$

The inert gas particles are assumed to utilize spherical drag parameters during dissolution into a mass source of liquid solute. Species transport is calculated using the multiphase flow model equations for bubble trajectories, force balance on each bubble, drag force on each bubble and particle Reynolds number [7]. The time it takes for the mixture to completely homogenize is known as the "mixing time". In this work, the recovery percentage is defined as follows:

$$C_m = 1 - \frac{C_{j, max} - C_{j, min}}{C_{j, max}}$$
 (14)

where  $C_{j, max}$  represents maximum alloy concentration in all 14 monitoring points. The time when  $C_m$  first reaches 95% is recorded as mixing time,  $t_m$ .

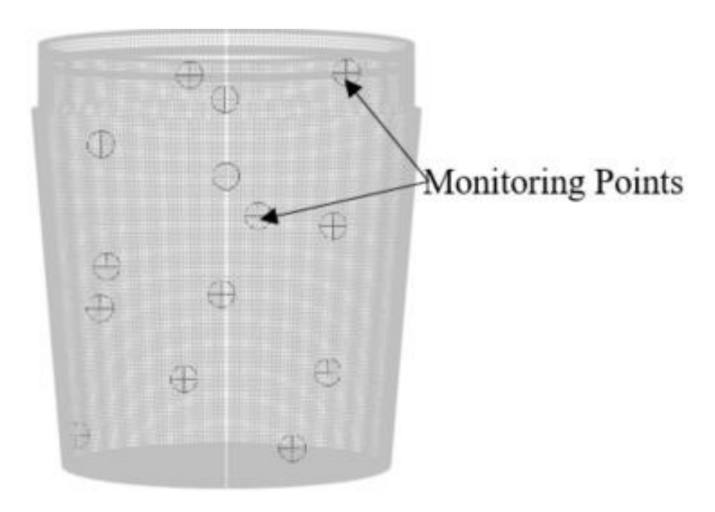
# 2.2. Simulation Procedures

The overall simulation is conducted using a two-step procedure, where the mixing study is carried out as the flow field reaches a quasi-steady state. Before the addition, the flow and turbulence calculations are deactivated, and particles are injected. In the plant, alloying is performed using bulk additions during tapping, powder injection using dense or dilute phase transport, or by wire-feeding to the ladle [13]. This investigation focuses on bulk addition, as it is widely practiced.

The injection location is mapped within the steel region at a calculated distance slightly below the slag eye. The air zone is set to a specified shear condition, with the DPM boundary condition set to escape. As shown in Figure 2, 14 locations across the whole ladle are marked for accurate analysis of mixing time. Figure 3 shows the schematic of ladle geometry.

In this study, quasi-steady state is defined as when velocity on three planes level off. The plane location is shown in Figure 4. As shown in Figure 5, velocity on the planes 1 to 3 level off around 40 s after gas blowing, and 40 s is considered as the time taken for a quasi-steady state to be achieved.

Metals **2023**, 13, 421 6 of 19



 $\textbf{Figure 2.} \ \ \textbf{Steel zone showing marked regions.}$ 

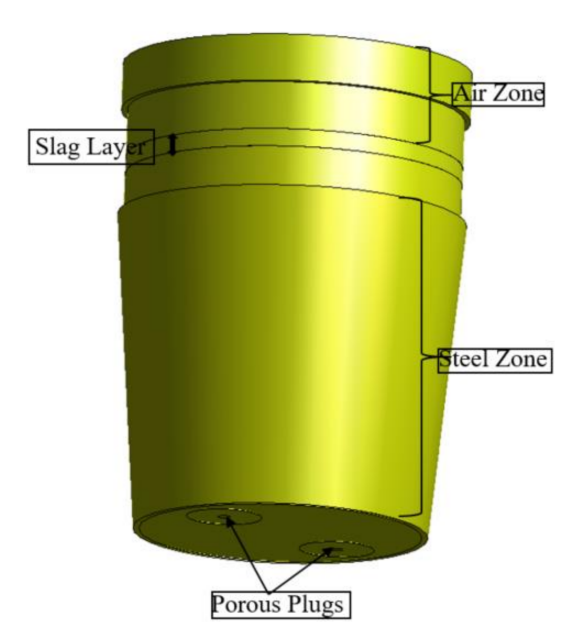


Figure 3. Ladle geometry.

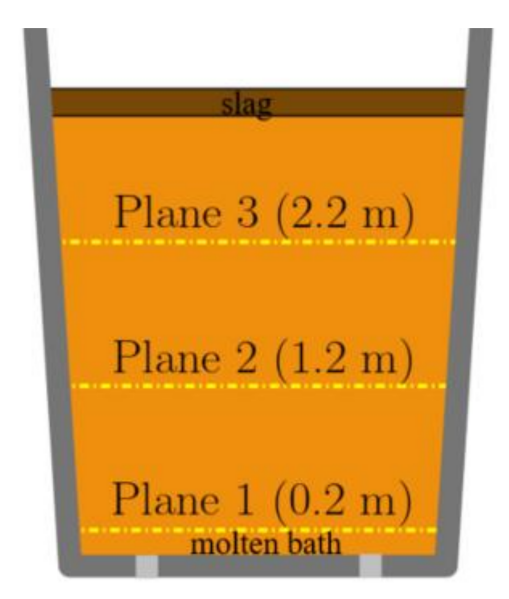


Figure 4. Positions of plane within the steel zone.

Metals 2023, 13, 421 7 of 19

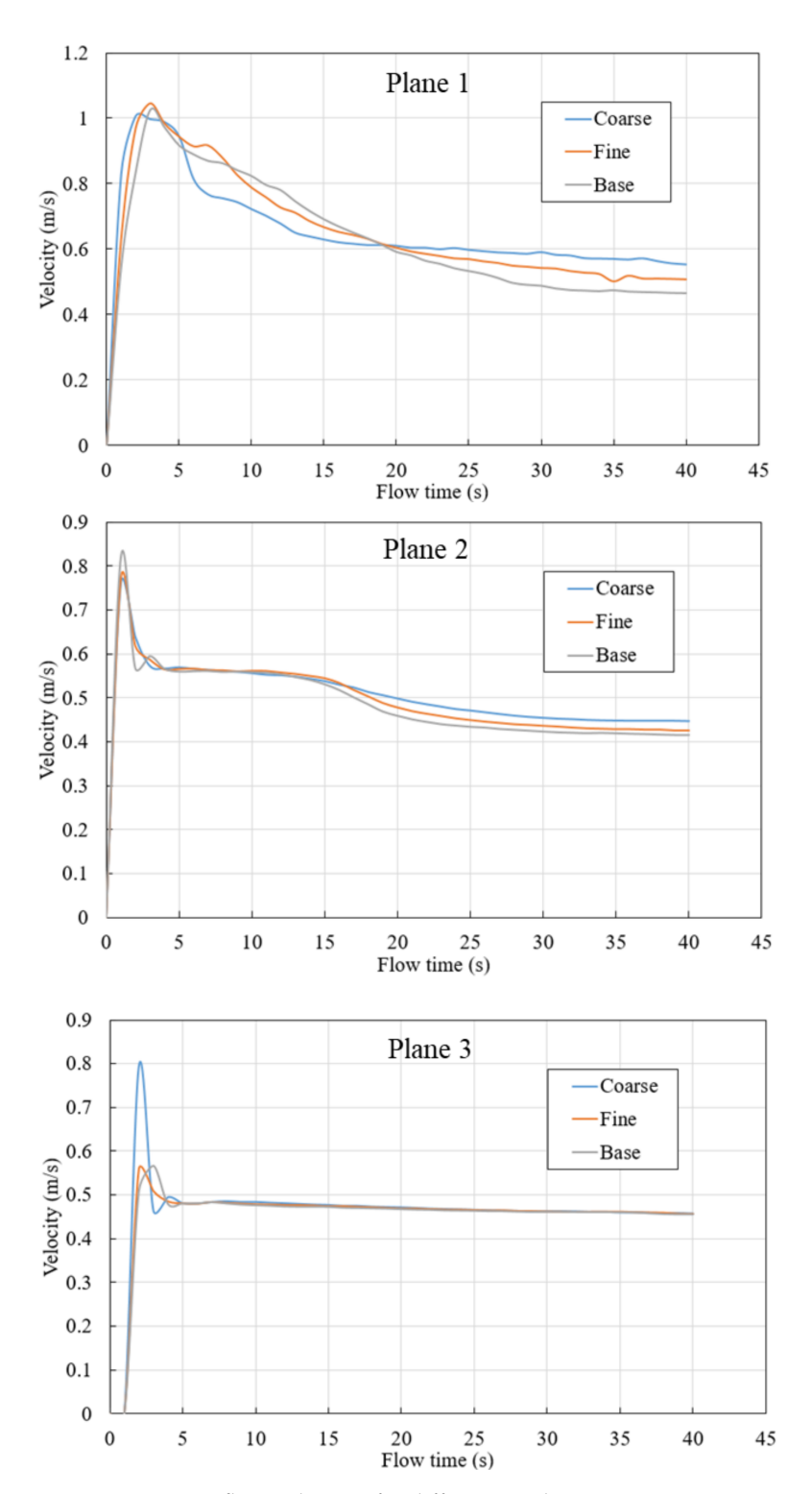


Figure 5. Average flow velocities for different meshes.

## 2.3. Computational Details

The domain depicted in Figure 3. Features a steel ladle comprising three zones: air, slag, and steel, with two porous plugs with a diameter of 0.104~m at the bottom. The steel heights and slag thicknesses are 3.23~m and 0.147~m, respectively. Inert gas flow rates of  $0.85~m^3/m$ in are used for each plug. In this case, the initial bubble diameter is 0.015~m. The walls are set to a no-slip boundary condition to capture the steep gradients with reasonable

Metals 2023, 13, 421 8 of 19

accuracy. The ladle top assumes particle escape, and a second-order implicit transient formulation is utilized for improved accuracy.

The grid created for the ladle's geometry is a structured hexahedral, possessing a fine cell count of approximately 1.6 million, replicated twice, with lesser cell counts of 1.2 million and 0.7 million, to study its effect on results obtained from the flow field. Table 1 shows the parameters utilized for computation.

Viscosity of liquid steel	0.0062 Pa.s
Surface tension of liquid steel [7]	1.4 N/m
Melt density	6795 kg/m <sup>3</sup>
Argon density	1.6 kg/m <sup>3</sup>
Slag density	2785.96 kg/m <sup>3</sup>
Specific heat of liquid steel [7]	820 J/kg.K
Thermal conductivity of liquid steel [7]	40.3 J/m.s.K
Diffusion coefficient of copper in liquid steel [18]	$6.4 \times 10^{-9} \text{ m}^2/\text{s}$
Diffusion coefficient of columbium in liquid steel [19]	$4.3 \times 10^{-9} \text{ m}^2/\text{s}$
Diffusion coefficient of vanadium in liquid steel [20]	$4.4 \times 10^{-9} \text{ m}^2/\text{s}$

Evaluation of the flow velocity was used to resolve the sensitivity for all three meshes on planes defined within the steel zone, as shown in Figure 4, characterized by height. Planes 1, 2, and 3 possess heights of 0.22 m, 1.22 m, and 2.22 m, respectively.

The plots in Figure 5 show average velocities across three different planes within the ladle. In the initial stages of the simulation, a large velocity peak can be seen in each plane as the rising bubble plume first reaches each plane's height within the ladle. However, as the simulation continues, the flow begins to recirculate within the ladle. This results in a downward flow that reduces the magnitude of the mean velocity in the measurement planes. Eventually, the flow reaches a quasi-steady state. As shown in Figure 5, the velocity from all meshes follows a similar trend; however, the base case is utilized for further investigation due to its computational efficiency and accuracy.

# 2.4. Model Validation with Plant Data

Models ranging from simplified assumptions to complex finite calculations have been built based on meticulous experimentation of the steel alloying procedure, with publications released likewise. Therefore, this work is validated with properties obtained from Nucor Steel.

The domain utilized as the base case for particle injection simulation was that of 1.2 million computing cells. Each porous plug is turned up to a maximum flow rate of  $0.85\,\mathrm{m}^3/\mathrm{min}$  during gas stirring to ease the charging of the alloys, which come in irregularly sized pellets of  $0.0064\,\mathrm{m}$  in diameter, added for  $30\,\mathrm{s}$ . The concentrations are measured each minute after addition to determine the amount recovered. Table 2 compares CFD model data against plant homogeneity test measurements.

A single injection is defined in a discrete phase at a downward velocity of 6 m/s on the y-axis. In this process, the dissolving alloy is copper. The residence time of copper is calculated based on Equation (9), and the initial steel temperature at the start of the homogeneity test is 1892 K. As each measurement is taken, there is a gradual reduction. The lowest recorded temperature is 1876 K, and liquidus is taken at 1805 K. The record of copper evolution over time is stated in Table 3. Samples are taken 7 inches below the top of the ladle from an established region within the axis of one of the CFD plugs, corresponding to the plant location.

Metals 2023, 13, 421 9 of 19

١.

Temperature (K)	Time (s)	Concentration: Plant Current/Initial	Concentration: CFD Current/Initial	Δ
1892	0	1.000	1.000	0.0%
1892	60	1.373	1.370	0.2%
1885	120	1.386	1.297	6.4%
1881	201	1.454	1.263	13.1%
1876	240	1.474	1.249	15.3%
1880	300	1.506	1.239	17.7%
1878	360	1.474	1.231	16.5%

Table 3. Case Matrix.

Case No.	Plugs	Flow Rates (Per Plug—m³/min)	Alloy
Case 1 (Base)	2	1.70 (0.85)	Copper
Case 2	2	1.13 (0.71 and 0.42)	Copper
Case 3	1	0.85 (0.85)	Copper
Case 4	2	1.70 (0.85)	Columbium
Case 5	2	1.70 (0.85)	Vanadium

The data is scaled based on initial alloy concentration:

$$C_S = \frac{C_j}{C_0} \tag{15}$$

Here,  $C_S$  represents the scaled alloy mass fraction,  $C_j$  and  $C_0$  is mass fraction at time j and the initial.

Data on scaled concentrations of copper obtained from the sample location in the plant are compared to those of the developed model at same location in Figure 6. The concentration at 0 s is set as 1. As we can see from the Figure 7 and Table 2, the difference between CFD prediction and plant measurement are summarized in three sections, they are 2.23%, 11.6%, and 16.5%. As mentioned in simulation procedures section, the alloy recovery simulation is performed when the flow and turbulence equation is deactivated ("frozen flow") in order to speed up the simulation. By using single two Rome CPUs at 2.0 GHz, the simulation speed is roughly 1 simulation seconds/actual hour with all equations activated. It will be speed up 45 times when flow and turbulence equation is deactivated. The difference between CFD and plant measurement may because of the frozen flow technique, but the total difference of 9.9% is acceptable. The same simulation technique will be applied for all flowing cases.

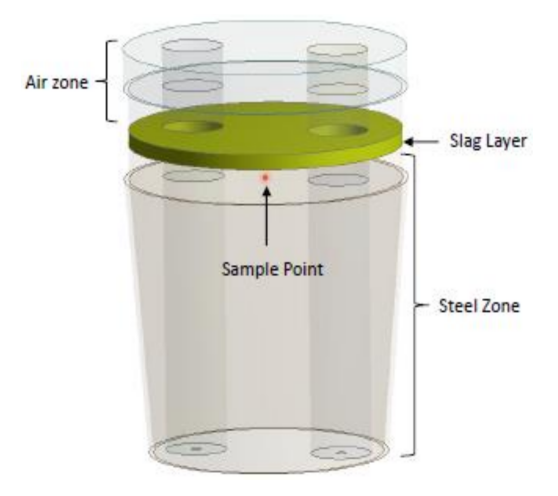


Figure 6. Sample location within steel zone.

Metals 2023, 13, 421 10 of 19

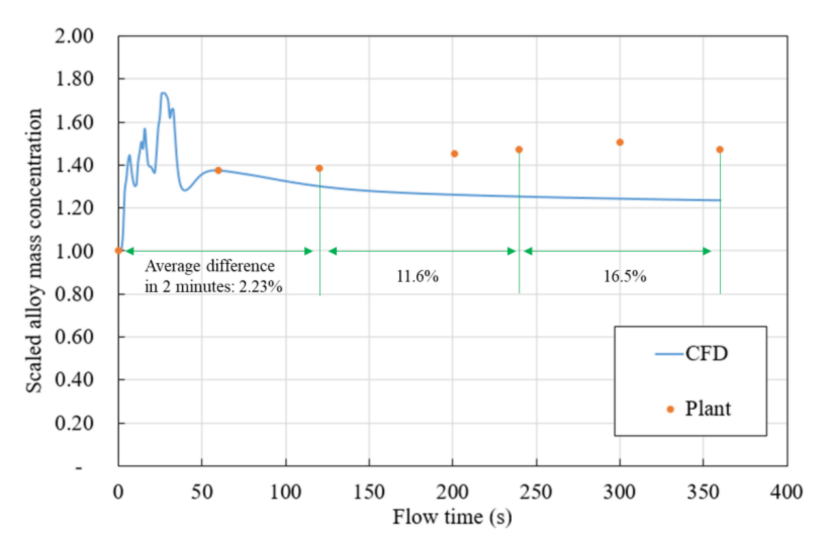


Figure 7. Scaled alloy mass concentration comparison (plant measurement–CFD).

## 3. Results and Discussion

In the following section, five cases will be discussed. The case matrix is shown below. As shown in Table 3, the effect of ladle plug design, flow rate, and different alloy types on mixing is compared and investigated.

## 3.1. Flow Field

As mentioned, three flow conditions are discussed. Figure 8 shows basic features, duo plug symmetric flow, of the flow pattern inside the ladle. The velocity contour at the centerline plane reveals that the recirculation in between the plumes and near the walls actively influences how fast and to what extent mixing occurs. Dead zones near the ladle bottom indicate low concentration fluctuations and analysis at the vortex core region, colored by velocity, reveals a gradient of energy-concentrated areas along the metal–slag interface.

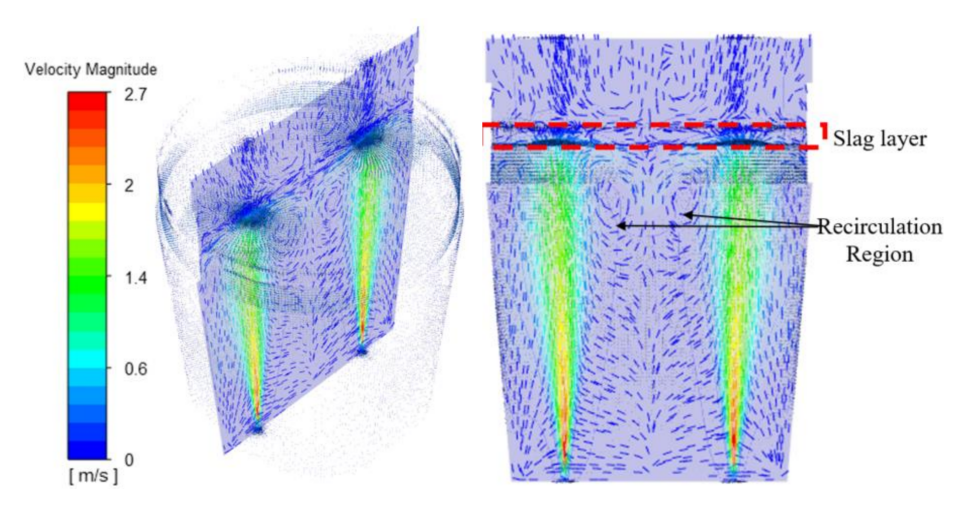


Figure 8. Velocity magnitude vector along the center plane showing areas of recirculation.

The local gradient at interface allows mixing, and the strain field expands the mixing region between the plumes. In addition, the flow intensity during the gas—liquid interaction of the plume creates slag eyes with a diameter of 0.66 m above plugs 1 and 2.

As shown in Figure 9, for dual-plug (case 1) and single-plug (case 3) ladles, mass-averaged velocities are compared based on plane 3. A dual-plug with a higher total flow rate can generate higher flow velocity.

Metals 2023, 13, 421 11 of 19

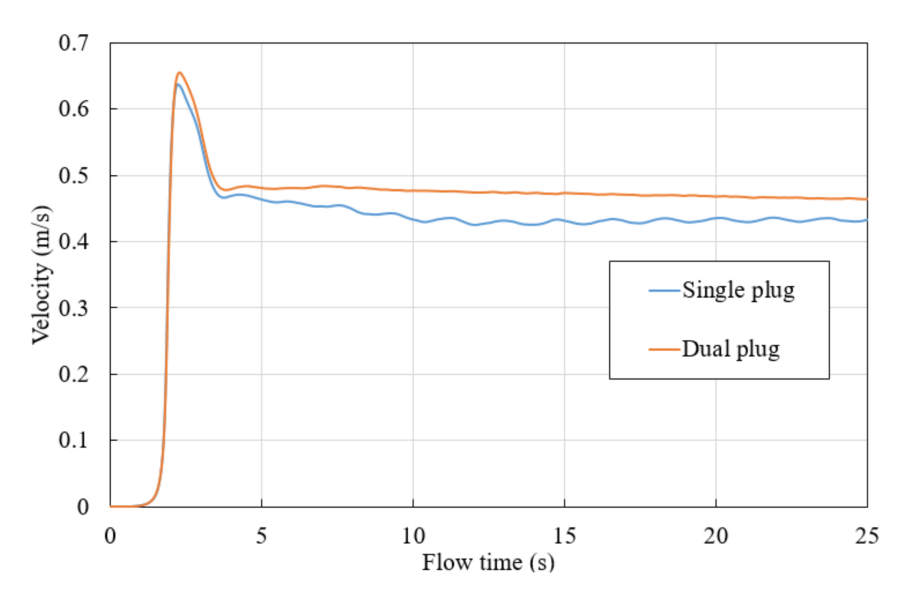


Figure 9. Flow velocities for single- and dual-plug ladles.

It is important to note that the cross-sectional area of the plume zone heavily influences circulating flow, and vector contours of velocity magnitude in Figure 10 distinctively show this difference in their flow pattern inside the ladle. Fluid flow tends more toward a higher flow rate plume. It can make alloy distribution more uneven throughout the domain.

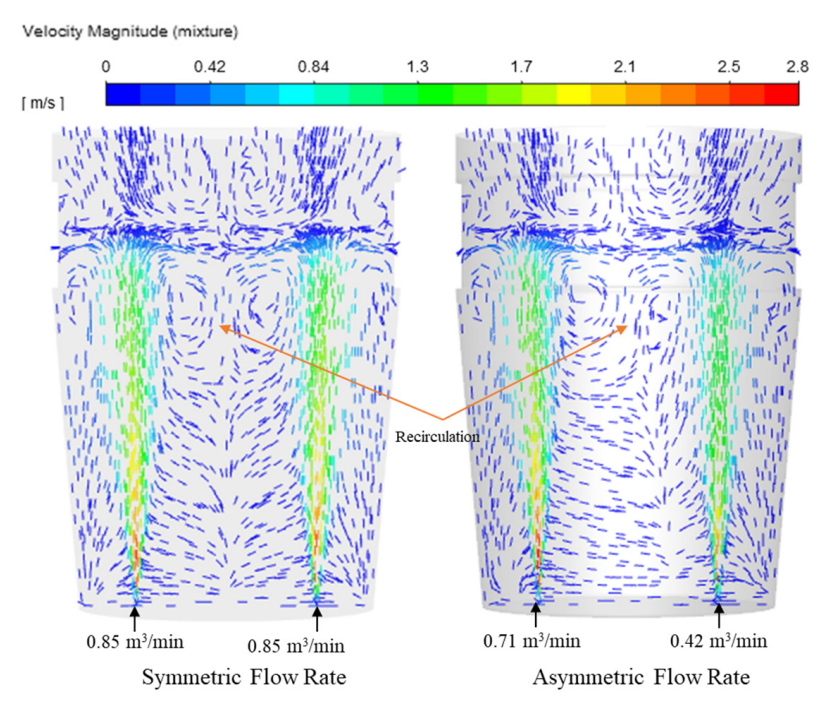


Figure 10. Vector contour of flow field.

## 3.2. Copper Particle Dissolution Behavior

The injection point is marked at 0.43 m below the slag—air interface, where particle velocity trajectory is tracked location-based as seen in Figure 11. There is no major displacement recorded at the point of emission except for the existing flow field plume momentum, which offsets the particle velocity by reducing it, causing them to spread outwards then slowly trail downwards, before dissolving into the melt after the critical time, tc, as seen in Figure 12.

Metals 2023, 13, 421 12 of 19

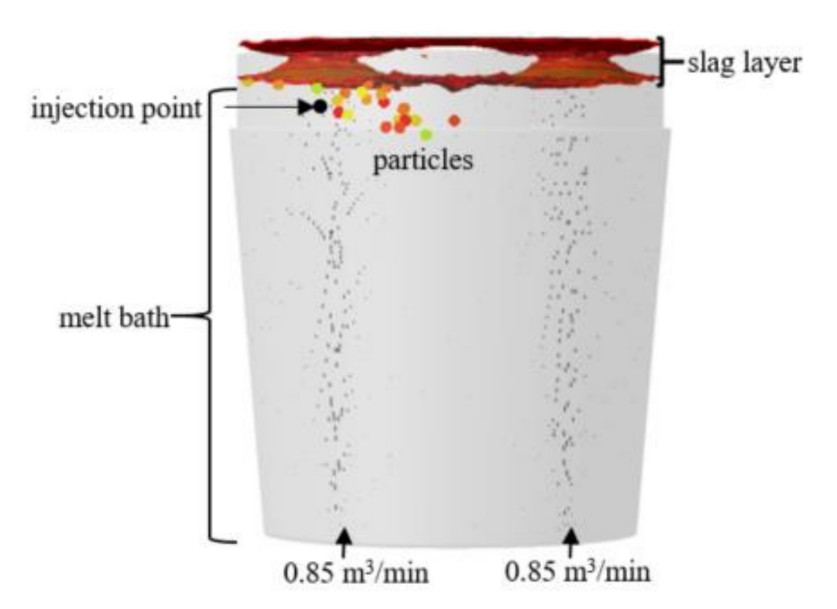


Figure 11. Particle release using point injection model.

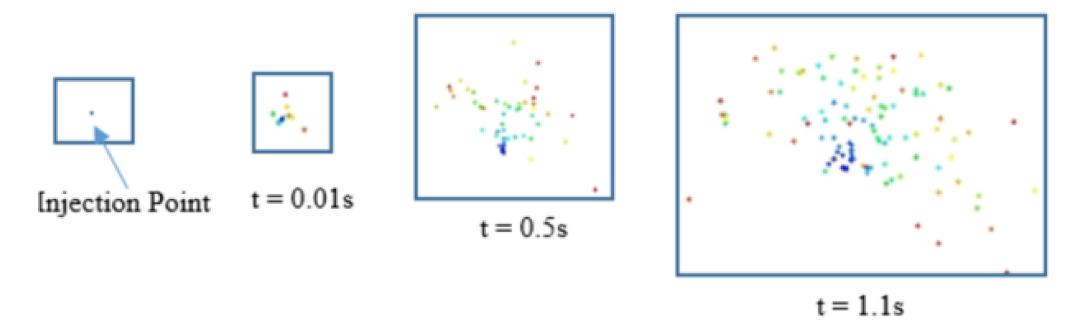


Figure 12. Particle behavior at injection point.

Similarities between the flow results for both dual-plug cases simulated extend to their critical time, which equals 1.14 s for the symmetric flow rate case and 1.13 s for the asymmetric flow rate case; critical time for the single-plug ladle is obtained at 1.05 s. After dissolution, particles remain within the continuous phase while the simulation continues runs until mixture homogeneity is obtained. Mixing time values for each simulation are different at 95% homogenization, as this is confirmed to depend on the gas flow rate.

## 3.2.1. Dual-Plug Ladle-Symmetric Flow

The time distribution of the particle release, shell formation, and species dissolution can be seen in the mass fraction contours in Figure 13. In the figure, the upper red region indicates the slag layer and slag eye shape. Due to the symmetry flow rate, the two slag eyes have a very similar shape and size. Investigation of the discrete phase velocity magnitude of the particles as they enter the liquid steel reveals a massive reduction. Since copper is denser than steel, the particles drop directly into the bath, gradually accumulating towards the center even as the injection occurs at the left plume. Though the initial speed is reduced due to steel movement and, of course, the existing momentum of the plume, it stays constant at approximately 0.8 m/s for the first 15 s of addition. More fluctuations are recorded, with the lowest speed of 0.11 m/s observed at 75 s.

From the injection point, the particles accumulate between the plumes and a shell of mass forms around the perimeter of the copper particles. After the critical time of 1.14 s, it melts, leaving the alloy to slowly dissolve and diffuse across the steel bulk, sinking towards the bottom.

Metals 2023, 13, 421 13 of 19

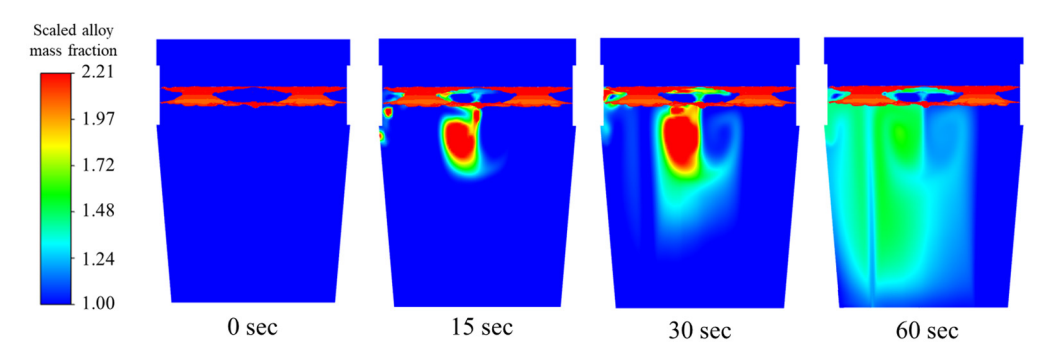


**Figure 13.** Mixing behavior of copper for 1.70 m<sup>3</sup>/min total flow rate.

# 3.2.2. Dual-Plug Ladle-Asymmetric Flow

For the asymmetric flow, slag eye size is different. Higher flow rate side generates larger slag eye. In this case, alloy is injected from larger slag eye area. From Figure 14, most of the recirculation seems to be pushed towards the higher flow rate, unlike the baseline flow, which shows centered recirculation regions between the plumes. As shown in Figure 14, recirculation drives for faster mixing; therefore, the same copper mass is injected into the flow field to observe the changes as the particles diffuse. The same behavior of the copper particles from the base case is seen; however, the cluster of mass formed in the melt is closer to the higher flow rate plume, exactly where the region of recirculation was noticed in the flow field prior to subsequent melting. The time it takes for the steel shell to melt, allowing the copper particles to dissolve is 1.13 s.

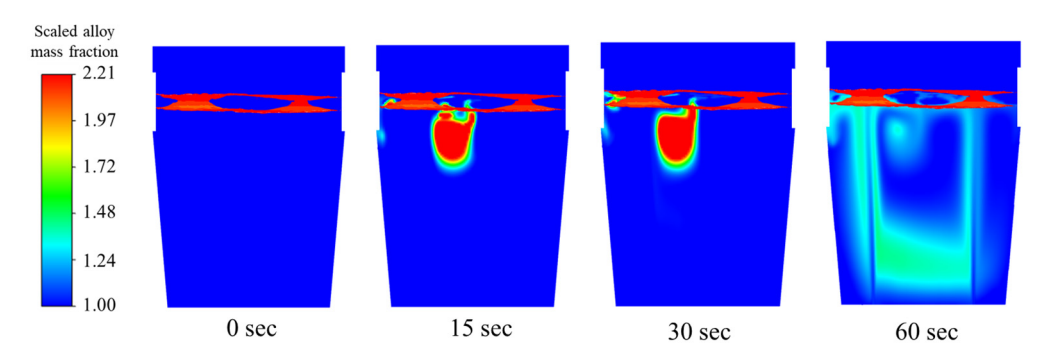


**Figure 14.** Mixing behavior of copper for 1.13 m<sup>3</sup>/min total flow rate.

At 60 s of mixing, the mass fraction of copper species can be seen to have almost totally diffused across the molten bath.

## 3.2.3. Single-Plug Ladle

Same point injection process is carried out here. From the contours in Figure 15, the copper mass can be seen to move towards the center even though the injection occurs within one plume. When the steel shell melts after 1.05 s, there seems to be a slow diffusion of the particles as they are gradually distributed downwards.

In all time variations of the contour plots below, there seem to be high concentrations of the copper mass fraction closer to the plume region, even as dissolution is occurring.

The exact sample location shown in Figure 6 from the base case was assigned to the above simulated cases and concentrations obtained in each simulation. The results are compared with each other in Table 4. Temperature of the melt fluctuates as the amount of copper recovered at every minute reduces with the increase in time as with the validated case. The results support that difference in circulation behaviors due to changes in number of plugs or reduced flow rate during stirring impacts flow turbulence in the ladle. This occurrence introduces percentage differs when concentrations at the same location are taken.

Metals 2023, 13, 421 14 of 19

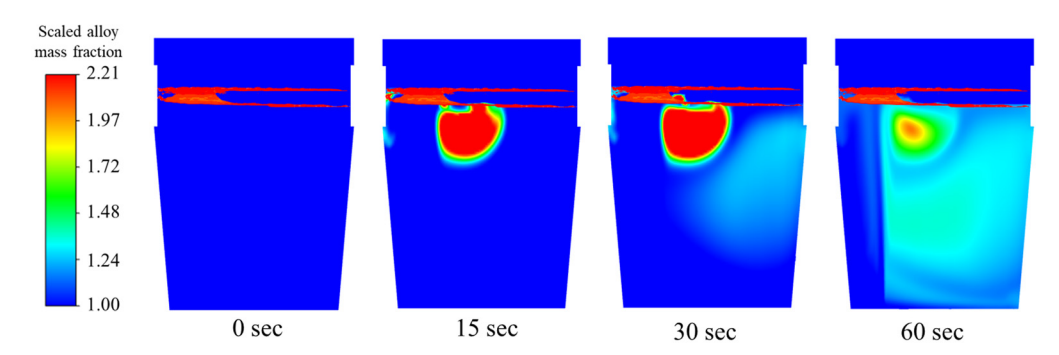


**Figure 15.** Mixing behavior of copper for 0.85 m<sup>3</sup>/min total flow rate.

**Table 4.** Scaled recovered copper concentrations on parametric studies.

Temperature (K)	Time (s)	Case 1 (Dual-Plug, 1.70 m³/min, C <sub>current</sub> / C <sub>inital</sub> )	Case 2 (Dual-Plug, 1.13 m³/min, Ccurrent / Cinital)	Case 3 (Single-Plug, 0.85 m³/min, C <sub>current</sub> / C <sub>inital</sub> )
1892	60	1.370	1.177	1.301
1885	120	1.297	1.150	1.290
1876	240	1.249	1.128	1.257
1880	300	1.239	1.129	1.254
1878	360	1.231	1.130	1.253

To conclude, these three scenarios, from Table 4, since initial concentration of each case is the same, case 2 (dual-plug with asymmetric flow) shows quicker mixing. It can also be found from Figures 13–15, at 60 s, in the lower part of the ladle and on the near-wall side away from the injection location, a higher concentration of alloy was observed in case 2. It means more alloy is descending to the lower part of ladle compared to the other two scenarios. The alloy mass fractions of case 1 and case 3 still showed higher concentrations near the injection point at 60 s.

## 3.3. Behavior of Vanadium (V) and Columbium (Cb) Alloying Elements

Vanadium (V) and columbium (Cb) particle behaviors in steel are observed and compared with that of the copper baseline simulation using same amount of particle mass. Their respective melting points, specific heat capacities, viscosities, and densities are utilized to obtain critical time of dissolution for each alloy. It is observed that the number of particles in a parcel is unique to a particular alloy, as the Fluent (2020 R1, ANSYS, Canonsburg, PA, USA) used recalculates it in adjustment to updated parameters, regardless of the defined mass.

Each alloy displays almost the same behavior during injection as represented in the respective time-varying mass fraction contours. Columbium possesses a relatively high melting point but has the shortest shell existence time of 0.758 s amongst all three microalloying elements. From the contours, rapid dissolution towards the ladle bottom is noticed after the shell melts, and concentration distribution is more intense and dispersed across the bath than copper, which could be attributed to its lower density.

During the dissolution of Cb in Figure 16, mass flux is controlled by the bath temperature, and the continued agitation of the melt considerably increases this mass flux.

Vanadium has high solubility even at temperatures lower than its melting temperature and is less dense than steel; therefore, over 90% of the addition is immersed in the bath, which lowers oxidation losses and speeds up breakdown. Again, this study does not emphasize the chemical reactions of this alloy within the molten steel. Recovery of the alloy can be very high when standard addition practices are utilized.

Metals **2023**, 13, 421 15 of 19

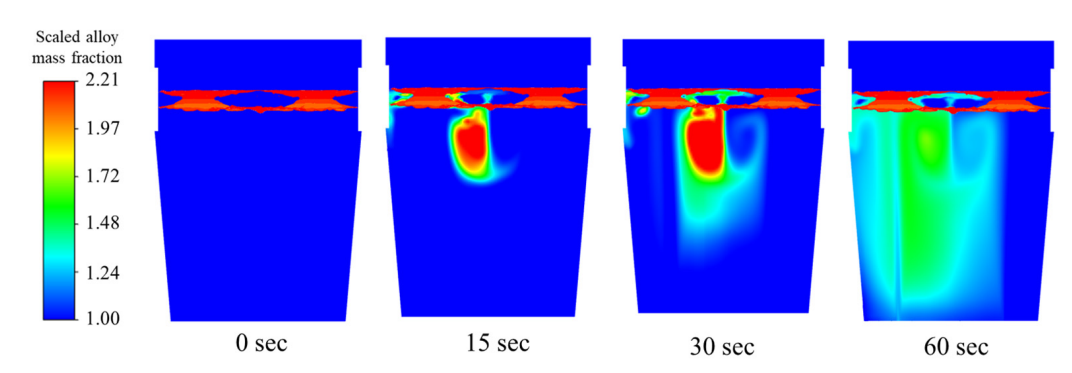


**Figure 16.** Mixing behavior of columbium alloy for 1.7 m<sup>3</sup>/min total flow rate.

The calculated time for shell existence is 1 s. According to mass fraction behavior seen in Figure 17, the cluster of mass is not as intense as that of the other alloys.

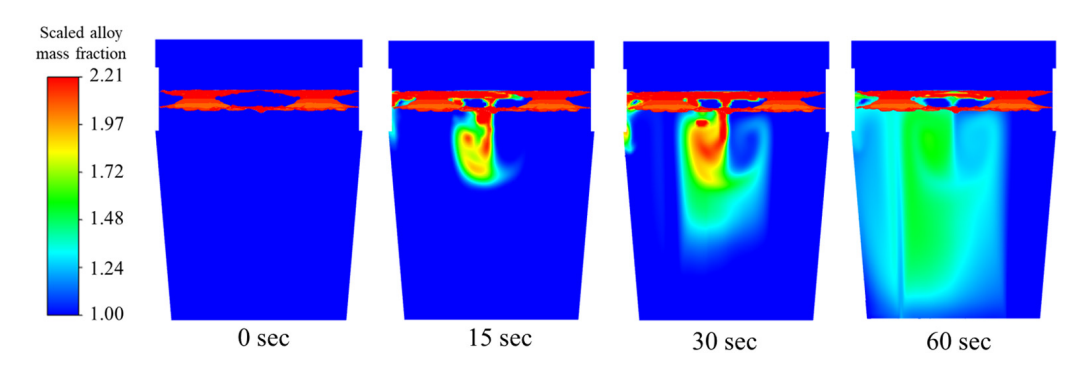


**Figure 17.** Mixing behavior of vanadium alloy for 1.7 m<sup>3</sup>/min total flow rate.

Table 5 record scaled alloy mass fraction for copper, columbium, and vanadium. It can be found at monitoring location; mass concentration of vanadium drops faster than other two alloy types. The detailed mixing behavior in the whole ladle can be found in next section.

Temperature (K)	Time (s)	Case 1 (Copper, C <sub>current</sub> /C <sub>inital</sub> )	Case 4 (Columbium, C <sub>current</sub> /C <sub>inital</sub> )	Case 5 (Vanadium, C <sub>current</sub> /C <sub>inital</sub> )
1892	60	1.370	1.354	1.321
1885	120	1.297	1.268	1.235
1876	240	1.249	1.226	1.196
1880	300	1.239	1.218	1.190

**Table 5.** Scaled mass fraction of alloy concentrations recovered.

360

# 3.4. Mixing Time

1878

Since recovery is a function of dissolution rate, alloy density, and dissolved oxygen in the melt [21],

1.231

$$R = f(u, \rho, [O]) \tag{16}$$

1.211

1.184

where R is recovery, u is solution rate,  $\rho$  is density and [O] is dissolved oxygen on liquid steel.

Concentrations of each alloy are collated from the exact sample point location as that of the plant. Table 5 show similar trend of reduced concentration as time of mixing increases for all three alloys evaluated showing the consistency of the model in defining the

Metals 2023, 13, 421 16 of 19

characteristic behavior of the particles. Copper was the most concentrated while vanadium had the least when compared to all three, which could be attributed to some of the particles attaching to the slag as a result of the initial flotation.

Determining the total mixing time when the normalized concentration reaches 95–100% homogeneity involves taking the variance of the concentrations obtained from the already established monitoring points. Figure 18 shows mass concentration status in 14 monitoring points for case 1. Monitor points is shown in Figure 2. Combined with Equation (13), a mixing time of 852 s (14.20 min) was recorded. For all other cases, the same procedure is applied. The results are listed in Table 6.

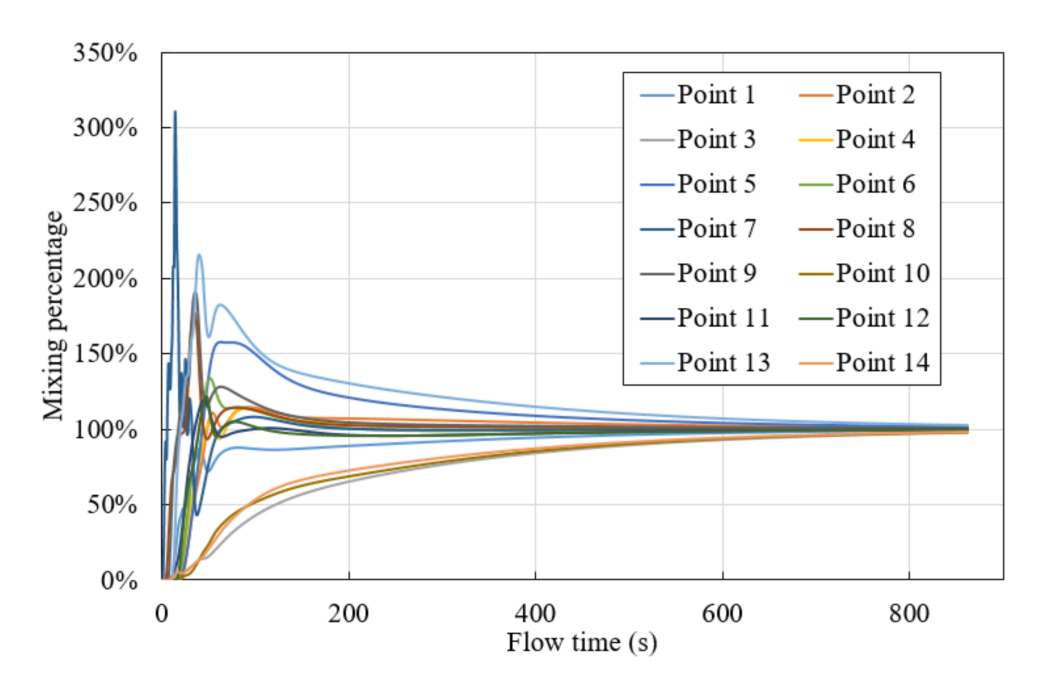


**Figure 18.** Point mixing percentage in case 1.

**Table 6.** Mixing time for each cases.

Cases	Total Flow Rate (Per Plug—m³/min)	Critical Time to (s)	Mixing Time (min)
No.1 Copper-dual-plug	1.70 (0.85)	1.14	14.20
No.2 Copper-dual-plug	1.13 (0.71 and 0.42)	1.13	5.56
No.3 Copper–single-plug	0.85 (0.85)	1.05	5.60
No.4 Columbium-dual-plug	1.70 (0.85)	0.76	13.83
No.5 Vanadium-dual-plug	1.70 (0.85)	1.00	13.45

As mixing time is a function of liquid depth, mean ladle radius, gravity, and gas flow rate, there may be time over prediction if some points are located within dead zones or in cases where the time is affected by the superheat.

From the results, it can be further concluded that case 2 (dual plugs, asymmetric flow) and case 3 (single plug flow) have the very similar mixing time, but the scaled mass fraction of case 2 drops faster than case 3. The mixing time of case 2 or case 3 is faster than case 1 (dual plugs, symmetric flow). By comparing Figures 13 and 14, the symmetry flow of a higher flow rate is preventing the alloy from descending to the lower part of ladle, and it can obviously slow down the homogeneity in the whole ladle. But by comparing Figures 13 and 14, the dead zone area in the dual-plug case is less than in the single-plug case, although the mixing study shows that case 2 and case 3 have similar mixing times.

Metals 2023, 13, 421 17 of 19

For the difference between alloys under the same flow condition, they have similar mixing times. This means that the mixing time is effected the by ladle design and operation condition rather than alloy type. In terms of the different alloys, vanadium requires the shortest gas stirring time, followed by columbium and copper.

## 4. Conclusions

Microalloy addition was simulated in a two-step process using a three-dimensional multiphase flow model. Gas stirring carried out at the first-stage revealed a zone of recirculation noticed between the plume pulses with an intensity close to the slag-metal interface and also pushing outwards towards the ladle walls. The pattern of the flow field obtained corresponds with plant observations. High charging of a dual-plug ladle for gas stirring was analyzed by comparing it with lower gas flow rates in the same and single-plug ladle to determine the necessity for an extremely high flow rate and invariably curb resource waste. Mixing behaviors of copper particles in all scenarios reveal that the process is heavily influenced by the recirculation generated around the plume during argon gas blowing, as the existing momentum slows the velocity at which the particles disperse from the point of alloy injection. One thing of note is that unconventional varied flow rate (asymmetric) gas stirring, when compared to standard same flow rates, results in shortened mixing time. Interestingly, the dual- and single-plug cases, with flow rates totaling 1.13 m<sup>3</sup>/min and 0.85 m<sup>3</sup>/min, respectively, arrived at the very similar mixing time. This result raises another level of curiosity for a fair comparison for these cases, where a total of 0.85 m<sup>3</sup>/min flow rate is to be simulated within a dual-plug ladle using the same or asymmetric flow charging pattern for each plug to ascertain if, indeed, the mixture will attain homogeneity at a shorter time.

The addition of copper as a high-strength, low-alloy steel for hydrogen-induced cracking suppression and corrosion resistance was further compared against other more common microalloying elements such as columbium and vanadium. The particle behaviors of these alloys reiterate the influence of density, specific heat capacities, and melting points on the critical or residence time that must exist before dissolution starts to occur. Moreover, the extensive turbulence and difference in circulation behavior for each particle results in variations in the amount of recoveries obtained at the sample point, which is expected.

In conclusion, based the condition in the study, a dual-plug asymmetric flow with total flow rate of  $1.13~\text{m}^3/\text{min}$  is suggested. Compared to copper, niobium, or vanadium, it can be blown for 30 s less. More studies can be conducted by using different alloys or varying the gas flow rate.

**Author Contributions:** Conceptualization, O.Q.D., X.G. and N.W.; methodology, O.Q.D. and X.G. software, O.Q.D., X.G. and N.W.; validation, O.Q.D. and X.G.; formal analysis, O.Q.D. and X.G.; investigation, O.Q.D. and X.G.; resources, C.Z.; writing—original draft preparation, O.Q.D. and X.G.; writing—review and editing, O.Q.D. and X.G.; supervision, N.W. and C.Z.; project administration, C.Z.; funding acquisition, C.Z. All authors have read and agreed to the published version of the manuscript.

**Funding:** This research was funded by National Science Foundation—GOALI, Grant Number: CMMI-2113967; and the Steel Manufacturing Simulation and Visualization Consortium (SMSVC).

**Data Availability Statement:** The data presented in this study are available on request from the corresponding author. The data are not publicly available because they were developed in the frame of a project with industrial partner.

**Acknowledgments:** The author is grateful for the opportunity to work on this project segment in collaboration with the National Science Foundation—GOALI (Grant CMMI-2113967). A massive thanks to the Steel Manufacturing Simulation and Visualization Consortium (SMSVC) members. Industry knowledge utilized for this study is based on the support from the Nucor Steel.

Conflicts of Interest: The authors declare no conflict of interest.

Metals 2023, 13, 421 18 of 19

#### Nomenclature

TOILCIC	iatuic
ho	Density of fluid, kg/m <sup>3</sup>
$\stackrel{ ho_A}{ ightharpoondown}$	Density of ferroalloy, kg/m <sup>3</sup>
$\overrightarrow{u}$	Local velocity, m/s
$F_b$	Force from bubble, N
k	Turbulence kinetic energy, m <sup>2</sup> /s <sup>2</sup>
ε	Turbulence dissipation rate, $m^2/s^3$
$Y_i$	Local mass fraction of species
$D_{i,m}$	mass diffusion coefficient for species i in the mixture
$S_i$	Source term of species i, kg m <sup>3</sup> /s
$D_{i,m}$ $S_{i}$ $\overrightarrow{F}_{VM}$ $\overrightarrow{F}_{pressure}$	Virtual mass force, N
É pressure	Pressure gradient force, N
Re	Reynolds number
$d_p$	Particle diameter, m
Q	Inert gas flow rate, m <sup>3</sup> /s
8	Acceleration of gravity, m/s <sup>2</sup>
$t_c$	Critical time to shell melting, s
Ср	Specific heat, J/kgK
$d_A$	Diameter of alloy particle, m
h	Heat transfer coefficient, J/m <sup>2</sup> sK
$T_{\mathrm{S}}$	Solidification temperature of the melt, K
$T_{\mathbf{M}}$	Temperature of the melt, K
$T_{\mathbf{O}}$	Initial temperature of alloy, K
$u_A$	Alloy velocity, m/s
$C_{pM}$	Heat capacity of melting steel, J/K
$k_M$	Thermal conductivity of molten steel, w/mK
Nu	Nusselt number
Pr	Prandtl number
$C_m$	Recovery percentage
$C_{j, max}$	maximum alloy concentration in all monitoring points
$C_{j, min}$	minimum alloy concentration in all monitoring points
$C_{j, min}$ $C_{S}$ $C_{j}$	Scaled alloy concentration
$C_{i}$	Alloy concentration at time j
$C_0$	Initial alloy concentration

#### References

- 1. Holappa, L. Secondary Steelmaking-Treatise on Process Metallurgy. Ind. Process. 2014, 3, 301–345.
- 2. Peranandhanthan, M.; Mazumdar, D. Modeling of Slag Eye Area in Argon Stirred Ladles. ISIJ Int. 2010, 50, 1622–1631. [CrossRef]
- 3. Väyrynen, P.; Holappa, L.; Louhenkilpi, S. Simulation of Melting of Alloying Materials in Steel Ladle; Swerea Mefos: Luleå, Sweden, 2012.
- 4. Haider, A.; Levenspiel, O. Drag Coefficient and Terminal Velocity of Spherical and Nonspherical Particles. *Powder Technol.* **1989**, 58, 63–70. [CrossRef]
- 5. Zhang, L.; Oeters, F. Mathematical Modeling of Alloy Melting in Steel Melts. Steel Res. 1999, 70, 128–134. [CrossRef]
- 6. Warzecha, M.; Hutny, A.; Warzecha, P.; Kutyła, Z.; Merder, T. Investigations of Dual Plug Argon Blowing for Efficient Mixing at Ladle Furnace Station. *Arch. Metall. Mater.* **2021**, *66*, 561–572.
- 7. Aoki, J.; Thomas, B.; Peter, J.; Peaslee, K. Experimental and Theoretical Investigation of Mixing in a Bottom Gas-Stirred Ladle. *AISTech Proc.* **2004**, *1*, 1045–1056.
- 8. Zhang, L.; Aoki, J.; Thomas, B. *Designing a New Scrap-Based Continuous Steelmaking Process Using CFD Simulation*; Association for Iron & Steel Technology: Warrendale, PA, USA, 2005.
- 9. Lee, Y.; Berg, H.; Jensen, B. Dissolution Kinetics of Ferroalloys in Steelmaking Process. Ironmak. Steelmak. 1995, 22, 486–494.
- 10. Den Boer, A. Characterization of Ferroniobium and the Thermodynamics and Kinetics of Dissolution of Niobium Compounds in Liquid Iron. Ph.D. Thesis, McMaster University, Hamilton, ON, Canada, 2013.
- 11. Webber, D. Alloy Dissolution in Argon Stirred Steel; Missouri University of Science and Technology: Rolla, MO, USA, 2011.
- 12. Peaslee, K.D.; Webber, D.S.; Randall, B. Alloy Recovery and Control in Steel Making. In *Scholar's Mine 2005 Materials Science and Engineering*; Missouri University of Science and Technology: Rolla, MO, USA, 2005.
- 13. Engh, T.A. Principles of Metal Refining: Mixing, Mass Transfer and Numerical Models; Oxford University Press: Oxford, UK, 2021.
- 14. Materials, A. Analysis of Microalloying Elements in Steel. 2020. Available online: https://www.azom.com/article.aspx? ArticleID=19894 (accessed on 1 January 2023).

Metals 2023, 13, 421 19 of 19

15. Diehl Tool Steel. Available online: https://www.diehlsteel.com/technical-information/effects-of-common-alloying-elements-insteel (accessed on 1 January 2023).

- 16. Johansen, S.T.; Boysan, F. Fluid dynamics in bubble stirred ladles: Part II. Mathematical modeling. *Metall. Trans. B* **1988**, 19,755–764. [CrossRef]
- 17. Whitaker, S. Forced Convection Heat ransfer Correlations for Flow in Pipes, Past Flat Plates, Single Cylinders, Single Spheres, and for Flow in Packed Beds and Tube Bundles. *AIChE J.* **1972**, *18*, 361–371. [CrossRef]
- 18. Butrymowicz, D.B.; Manning, J.R.; Read, M.E. Diffusion in copper and copper alloys. Part III. Diffusion in systems involving elements of the groups IA, IIA, IIIB, IVB, VB, VIB, and VIIB. J. Phys. Chem. Ref. Data 1975, 4, 177–250. [CrossRef]
- 19. Sismanis, P.G. The Dissolution of Niobium and Zirconium in Liquid Steel. Ph.D. Thesis, McGill University, Montreal, QC, Canada, 1987.
- 20. Argyropoulos, S.A. Dissolution of High Melting Point Additions in Liquid Steel. Ph.D. Thesis, McGill University, Montreal, QC, Canada, 1981.
- 21. Argyropoulos, S.A. The Solution Rate and Recovery of Ferroalloys. Available online: https://www.pyrometallurgy.co.za/InfaconV/120-Argyropoulos.pdf (accessed on 1 January 2023).

**Disclaimer/Publisher's Note:** The statements, opinions and data contained in all publications are solely those of the individual author(s) and contributor(s) and not of MDPI and/or the editor(s). MDPI and/or the editor(s) disclaim responsibility for any injury to people or property resulting from any ideas, methods, instructions or products referred to in the content.